Final Draft

of the original manuscript

Mo, N.; McCarroll, I.; Tan, Q.; Ceguerra, A.; Liu, Y.; Cairney, J.; Dieringa, H.; Huang, Y.; Jiang, B.; Pan, F.; Bermingham, M.; Zhang, M.-X.:

Understanding solid solution strengthening at elevated temperatures in a creep-resistant Mg–Gd–Ca alloy.

In: Acta Materialia. Vol. 181 (2019) 185 - 199.
First published online by Elsevier: 01.10.2019

https://dx.doi.org/10.1016/j.actamat.2019.09.058

Understanding solid solution strengthening at elevated temperatures in a creep-resistant Mg-Gd-Ca alloy

Ning Mo[a], Ingrid McCarroll[b], Qiyang Tan[a], Anna Ceguerra[b], Ying Liu[b], Julie Cairney[b], Hajo Dieringa[c], Yuanding Huang[c], Bin Jiang[d], Fusheng Pan[d], Michael Bermingham[a], Ming-Xing Zhang,[a,*]

[a] School of Mechanical and Mining Engineering, The University of Queensland, St Lucia, QLD 4072, Australia

[b] Australia Centre for Microscopy and Microanalysis and School of Aerospace, Mechanical & Mechatronic Engineering, The University of Sydney, Sydney, NSW 2006, Australia

[c] MagIC-Magnesium Innovation Centre, Helmholtz-Zentrum Geesthacht, 21502, Germany

[d] College of Materials Science and Engineering, Chongqing University, Chongqing, 400030, China

* Corresponding author: Ming-Xing Zhang, 61-7-3346 8709, mingxing.zhang@uq.edu.au.

Keywords: Magnesium alloy; Mechanical properties; Atom-probe tomography; STEM HAADF

Abstract

The present work studies the strengthening mechanisms of a creep-resistant Mg-0.5Gd-1.2Ca (at.%) alloy at both room and elevated temperatures. Although peak-ageing (T6) at 180 °C for 32 h led to a significant increase in room temperature strength due to the precipitation strengthening by three types of precipitates (Mg_2Ca, Mg_5Gd on prismatic planes and a new type of Mg-Gd-Ca intermetallic compound on the basal plane), the as-solid solution treated (T4) alloy exhibited better resistance to temperature softening during compression and to stress relaxation at 180 °C and better creep resistance at 210 °C/100 MPa. The Gd-Ca co-clusters with short-range order in the Mg solid solution, which was verified, at the first time, by atom probe tomography (APT) analysis and atomic-resolution high angle annular dark field-scanning transmission electron microscopy (HAADF-STEM), were responsible for the solid solution hardening, offering a more effective strengthening effect through local order-strengthening. Such solid solution strengthening increased the thermal stability of the alloy structure at elevated temperatures, at least at early stage of the creep. Subsequently, dynamic precipitation started contributing to the creep resistance due to the formation of higher density of precipitates. However, in the T6 alloy, creep testing at elevated temperatures, particularly at 210 °C that was higher than the ageing temperature, led to coarsening of the precipitates, which acted as over ageing. As a result of such over ageing, the resistance of the T6 alloy to heat-induced softening was weakened, leading to lower creep resistance than the T4 alloy.

1. Introduction

Achieving high-temperature strength and creep resistance in magnesium alloys is widely accepted to be one of the principal challenges that must be overcome for their use in applications such as powertrain components in automobiles [1-2]. Magnesium-rare-earth (Mg-RE) based alloys, typically containing Gd, Y, Nd and Ce, are an important step towards creep-resistant Mg alloys, as they have been reported to have greater high-temperature strength and creep resistance than other Mg systems produced by either high pressure die-casting (HPDC) or gravity casting [3-7]. So far, the development of creep-resistant Mg-RE alloys has focused and relied on the strengthening effect offered by metastable precipitates, e.g. base-centred orthorhombic β' and face-centred cubic $\beta 1$ precipitates, which exhibit less diffusivity and good coherency to the Mg matrix [8-13]. However, to ensure appreciable volume fraction and satisfactory configuration for the precipitates to be effective, large amounts of RE are required, which increase the alloy cost significantly [12, 13]. It is therefore of commercial interest to reduce the RE additions in Mg-RE based alloys.

Although solid solution strengthening by RE solutes has been known as a predominate mechanism enhancing the creep resistance of Mg alloys, distinct to precipitation strengthening, the effect of solid solution still remains outstanding even RE concentration is low (≤1at.%). Suzuki et al. [14] reported that the minimum creep rate of the solid solution treated Mg-0.2Y (at.%) alloy was one order of magnitude lower than that of the Mg-3Al (at.%) alloy at 277 °C. Gravras et al. [15] recently found that the solid solution treated HPDC Mg-0.45La-1.18Y (at.%) alloy had higher creep resistance at 177 °C than the Mg-0.45La-0.63Nd (at.%) alloy, even though dynamic precipitation of β' and β_1 was observed in the latter. These results showed the importance of solid solution strengthening in supressing the creep of the low-RE Mg alloys. However, the problem remains that conventional elastic interaction fails to explain the abnormally higher solid solution strengthening of RE solutes compared to other solutes in Mg. It was pointed out by Maruyama et al. [16] that the solute-atmosphere dragging model was unable to explain the prominent difference in creep rate between Mg-Al and Mg-Y solid solution alloys since the atomic size misfit of Y (+11%) and Al (-12%) in magnesium were similar. Recent works by Gao et al. [17, 18] also reported that the solid solution strengthening rate $d\sigma/dC$ of Gd and Y atoms in Mg were higher than that of Zn and Al atoms, despite the apparently larger shear modulus misfit and atomic size misfit for Zn and Al.

Abaspour et al. [19, 20] investigated the high-temperature behaviours of Mg binary alloys containing 1 at.% of various solutes. The results demonstrated that RE elements (Gd, Y

and Nd) and calcium (Ca) had much higher solid solution strengthening effects than other commonly used solutes, such as Al, Zn and Sn, in Mg. It was proposed by Abaspour et al. [19] that the higher solid solution strengthening effect of the RE elements and Ca could be attributed to a short-range order strengthening effect in Mg solid solutions. Based on this outcome, a recent work by the authors used Ca to partially replace the Gd and developed a new cast Mg alloy of Mg-0.5Gd-1.2Ca (at.%) [21]. After solid solution treatment, this alloy showed compatible strength and improved stress-relaxation resistance at 180 ° C when compared with the alloy containing double content of Gd, Mg-1Gd-0.4Zn-0.2Zr (at.%) [22]. This result verified the comparable solute strengthening effect of Ca with Gd, which represents a new approach to reduce the usage of RE in development of creep-resistant Mg alloys [21]. In addition, Ca has been known that can increase the creep resistance of magnesium alloys due to the formation of intermetallic compound, Mg_2Ca, with a high melting point [23]. Therefore, the ternary Mg-0.5Gd-1.2Ca alloy exhibited great potential in high-temperature structural applications.

Nevertheless, to actually explore the Mg-Gd-Ca new alloy system, several unsolved questions need to be answered [19-21]. (1) What is the actual mechanism that results in higher solid solution strengthening effect of Gd and Ca than other commonly used solutes in Mg alloys, such as Al, Zn and Sn. Although Abaspour and co-workers [19, 20] considered that the short-range order governs the creep behaviours of low-RE Mg alloys, there is lack of direct experimental evidence proves the existence of short-range order in the as-solid solution treated Mg alloys. (2) It has been known that additions of Gd and/or Ca improve the creep resistance of Mg alloys, but, the creep behaviour of the Mg-Gd-Ca alloys still remains unknown. (3) Due to the low level of solute addition in the Mg-0.5Gd-1.2Ca alloy, whether does precipitation strengthening contribute to the enhancement in creep resistance of the alloy? The present work aims to investigate the high-temperature strength and creep resistance of the newly developed Mg-0.5Gd-1.2Ca (at.%) alloy, and to understand the strengthening mechanism of the alloy at elevated temperatures through microstructural examination using both aberration-corrected scanning transmission electron microscopy (STEM) and atom probe tomography (APT). The results also provide a better understanding of the factors that govern creep behaviour of in low-RE Mg alloys.

2. Experimental procedure

2.1 Material preparation

The nominal composition of the alloy was Mg-3Gd-2Ca (wt.%) which corresponds to Mg-0.5Gd-1.2Ca (at.%). This alloy was prepared through melting commercial purity (≥99.98%) Mg in a mild steel crucible in an electric resistance furnace, with the protection of a shielding gas of 1 vol.% SF6 - 49 vol.% CO2 - 50 vol.% dry air at 730 °C, followed by adding appropriate amounts of Mg-Gd and Mg-Ca master alloys. After isothermally holding for 20 minutes, the melt was cast into steel moulds (50 mm in diameter and 80 mm in length) that had been preheated at 200 °C. An Mg-9Al (wt.%) alloy was also prepared using pure Mg and pure Al following the same procedure.

Samples of the Mg-3Gd-2Ca (wt.%) alloy were cut from the middle section of the ingots. Two thirds of the samples were then solid solution treated at 510 °C for 16 hours in an argon atmosphere, followed by quenching into 70 °C water. Following previous work [19], in which all mechanical tests were conducted at 180 °C, some solid solution treatment samples were aged at 180 °C for various times to identify the peak ageing condition. Then, as-cast, solid solution treated and peak aged samples were machined to 9 mm in diameter and 18 mm high cylindrical specimens for compression and creep testing. Samples of the Mg-9Al (wt.%) alloy were cut from the middle of the ingot and solid solution treated at 412 °C for 16 h in the same argon atmosphere [24, 25].

2.2 Mechanical property and creep tests

Vickers microhardness was measured using a microhardness tester with a 1 kg load. The average of at least five measurements was used as the hardness value. Compression tests were carried out on a screw-driven Instron 4505 machine equipped with an environmental chamber that can be heated from 25 °C to 180 °C with a crosshead speed of 0.08 mm/min (initial strain rate = $7.5\times10^{-5}\ s^{-1}$). Sequential stress relaxation tests at 180 °C were conducted on the same machine. After compressing the samples to stress levels of 135 MPa, 175 MPa and 205 MPa at an applied crosshead speed of 0.2 mm/min (initial strain rate = $1.85\times10^{-4}\ s^{-1}$), the loading was stopped allowing the stress to relax for 1800 seconds (30 min). The stress relaxations were recorded and the difference in stress between the initial compression stress and the relaxed stress represents the resistance of the alloy to the stress relaxation. Creep tests were conducted with an ATS Lever Arm Test System at a constant compressive stress of 100 MPa at 210 °C. Each creep test was performed until either the specimen broke or the minimum creep rate was reached.

2.3 Microstructural characterization

The microstructure of the heat-treated samples was characterized using optical microscopy, transmission electron microscopy (TEM), atom probe tomography (APT) and high-angle annular dark-field scanning transmission electron microscopy (HAADF-STEM). The concentration profile of Gd and Ca in the Mg-matrix of alloys was determined through an electron probe microscope analysis (EPMA), conducted on a JEOL PROBE-8200 operated at 40 kV and 3.0 x 10^{-8} A. Samples for EPMA were mechanically ground and polished with 0.3 μm diamond suspension. For optical microscopy these samples were further etched in a 4 % nital solution (4 % nitric acid and 96 % ethanol). TEM thin foils of 3 mm diameter were mechanically ground to a thickness of 60 μm followed by ion milling in a precision ion polishing system (PIPS) operated at 5 kV accelerating voltage and 5 ° incident angle. A FEI Tecnai G2 F20 TEM, operated at an acceleration voltage of 200 kV, was used to examine the precipitates in the solid solution treated (T4 condition) and peak aged (T6 condition) samples. The number densities of precipitates were estimated by the methods described by Kelly [26] while the average size was measured following the description by Underwood [27]. Atomic-resolution HAADF-STEM images were obtained from a FEI Themis-Z double-corrected S/TEM operating at 300 kV. HAADF-STEM image is also known as atomic number (Z) contrast image, with its contrast depend highly on Z in a form of $Z^{1.6\text{-}1.9}$, making it easy to distinguish different atomic columns. The point resolution under this imaging mode is approximately 0.6 Å. The collection semi-angle was 48-200 mrad. All HAADF-STEM images were processed by masking of diffraction spots in the fast-Fourier transform of the original images and then inverse-transforming using Gatan Digital Micrograph.

Atom probe specimens with dimensions of 0.5×0.5×20 mm^3 were cut from bulk samples and carefully ground. Samples were then polished into a needle-like shape using a two-stage, double-layer and electro-polishing process [28]. Initial rough polishing was conducted in an electrolyte of 25 vol.% perchloric acid and 75 vol.% glacial acetic acid at ~19-21 V. Final polishing was conducted in a 2 vol.% perchloric acid and 98 vol.% 2-butoxy-ethanol electrolyte at 15 V. APT analysis was carried out on a CAMECA Local Electrode Atom Probe (LEAP) 4000X Si operated at a temperature of 40 K, with a pulse frequency of 250 kHz and a pulse energy of either 50 or 100 pJ, pulse energies were chosen to balance the quantity of data obtainable and the quality of the resulting mass spectrum. A detection rate of 1.0 % was used. Tomographic reconstruction and visualization of the APT data was performed using IVAS version 3.6.12. Cluster analysis was performed by using the contingency table analysis (CTA) and generalized multicomponent short-range order (GM-

SRO) software package on the Atom Probe Workbench of the Characterisation Virtual Laboratory [29].

3. Results

3.1 Ageing response of the cast Mg-0.5Gd-1.2Ca alloy

As Mg-Gd-Ca system is heat-treatable, the ageing response of the Mg-0.5Gd-1.2Ca alloy was investigated. Fig. 1a presents the age-hardening curve at 180 °C for the Mg-Gd-Ca alloy after solid solution treatment at 510 °C for 16 hours. Peak ageing was achieved at 32 hours with a hardness of 66 HV. Optical micrographs of the as-cast, solution treated and peak-aged alloys are shown in Figs. 1b-d. It can be seen that solid solution treatment at 510 °C for 16 hours dissolved the majority of intermetallic phases. Further aging improved the hardness due to the formation of much finer precipitates, which caused the discolouring of the grains in Fig. 1d.

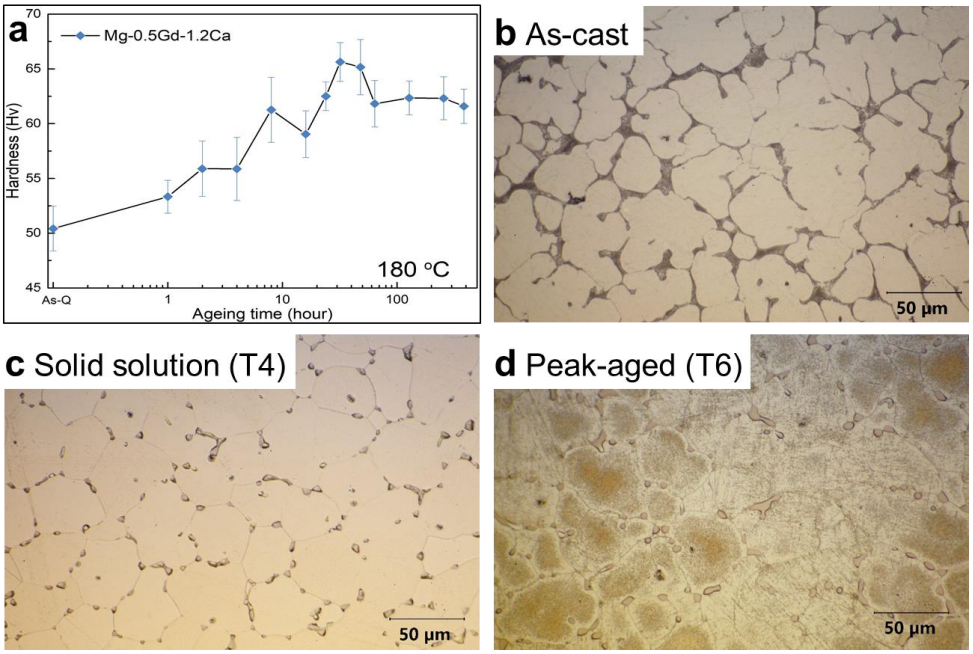

Figure 1 (a) Aging-hardening curve of the cast Mg-0.5Gd-1.2Ca at 180 °C after solid solution treatment at 510 °C for 16 hours; Optical micrographs of (b) the as-cast; (c) solid solution treated; and (d) peak-aged Mg-0.5Gd-1.2Ca alloy.

3.2 Mechanical properties

Figs. 2a and 2b show typical compressive strength curves of the alloy at both room temperature and high temperature (180 °C) for as-cast, solution treated (T4) and peak-aged (T6) samples. When compressed at room temperature, the solid solution strengthening in the T4 alloy offered a moderate improvement in the strength, with only 15 MPa increment of the

ultimate strength (US) compared with the as-cast sample. But peak ageing led to noticeable increase in both yield strength (from about 95 MPa to about 150 MPa) and US (from 236 MPa to 272 MPa) when compared with the T4 alloy. This result indicates that precipitation strengthening contributed to the room temperature strength of this Mg alloy containing both Ca and the Gd. However, when the compression test was done at 180 °C, as expected, both the YS (from 160 MPa to 120 MPa) and US (from 272 MPa to 220 MPa) of the T6 alloy were obviously reduced. But the testing temperature exhibited little impact on the strength of the T4 alloy. Both the YS and US tested at 180 °C remained the same as those at room temperature. In addition, serrated flow, indicative of the Portevin-LeChatelier (PLC) effect, can be clearly seen on the compressive flow curves of the T4 alloy, especially at high temperature. Such phenomenon has been commonly reported in the Mg-Gd and Mg-Y alloys [3, 15, 21, 30], as a result of the dynamic interaction between solutes and gliding dislocations. Generally, metals show lower strength at higher temperatures, the same strength (YS and US) of the T4 alloy at room temperature and at 180 °C could be attributed to following two possible reasons: 1) that solid solution strengthening plays the predominate role in strengthening these two alloys, with equivalent strengths at 180 °C and room temperature implying that solid solution strengthening is more thermally stable than precipitation strengthening, or 2) that precipitation occurs during compression testing, which compensates for the loss of strength due to the temperature increase. Microstructural characterization was performed in Section 3.3 to clarify which of these two factors was critical to the thermally stable strengthening of this T4 alloy.

Compressive stress relaxation and creep behaviours at 180 °C are shown in Figs. 2c-f. From Fig. 2c, one can see that, after compression ceased at a true stress of 205±5 MPa at 180 °C, the stresses relieved in 30 min were 9.2 MPa for the T4 alloy, 12.6 MPa for the T6 alloy and 22.1 MPa for the as-cast alloy. This result indicates that the T4 alloy had the highest stress relaxation resistance, followed by the T6 alloy, with the as-cast alloy having the lowest stress relaxation resistance at high temperatures. Similar results were observed for 30 min stress relaxation tests at true stresses of 135±5 MPa and 175±5 MPa at 180 °C, as shown in Fig. 2d.

It is well-accepted that stress relaxation is a phenomenon which is closely related to creep, proceeding by the same mechanism as creep [31-34]. To further verify the stress relaxation results, compressive creep tests were conducted. In order to shorten the testing period, the creep test was undertaken at a higher temperature, 210 °C, with an applied stress

of 100 MPa. Fig. 2e shows the creep curves of the T4 and T6 alloys. The creep consisted of the primary creep stage and the steady-state creep stage. The curves of primary stage within 20 hours is enlarged in the Fig. 2f. It can be seen that although the creep behaviour of both the T4 and T6 alloys is very similar at initial stage of the creep (within 2 hours), the T4 alloy showed much lower creep strain after forward than the T6 alloy. At the steady-state creep stage, the minimum creep rates ($\dot{\varepsilon}$) were measured as 1.96 x 10^{-8} s^{-1} for the T4 alloy and 4.92 x 10^{-8} s^{-1} for the T6 alloy. Obviously, the T4 alloy exhibited overall better creep resistance than the T6 alloy. Continuing creep testing at 210 °C led to over ageing of the T6 alloy, weakening its resistance to creep strain, and to ageing effect of the T4 alloy, enhancing the resistance to creep strain. Particularly, at the primary stage, the T4 alloy was still solute supersaturated even though the ageing might start. Hence, the cooperative effects of the solid solution and dynamic precipitation strengthening enhanced the creep resistance of the T4 alloy.

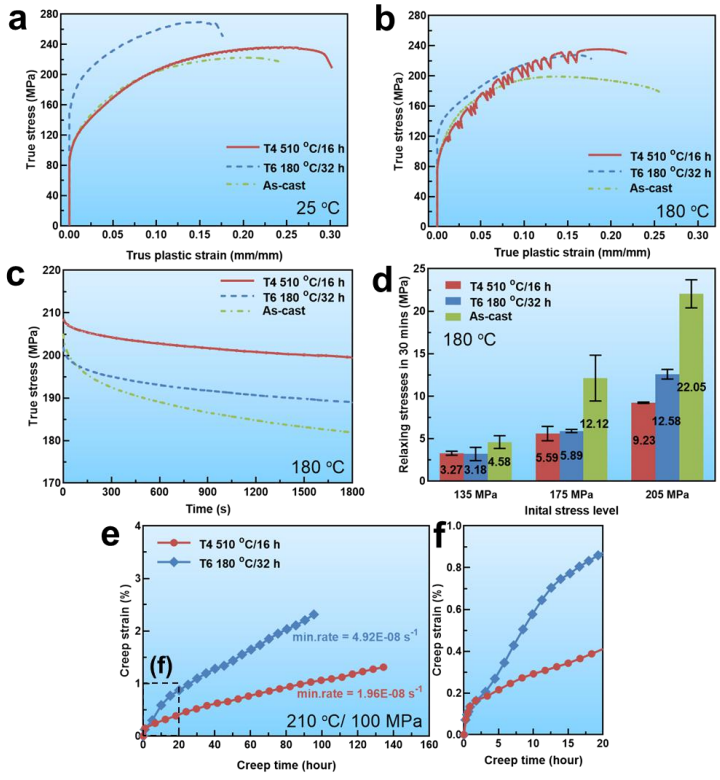

Figure 2 Compression and creep properties of the as-cast, T4 (solution treated) and T6 (peak aged) alloys: (a) compressive curves at room temperature; (b) compressive curves at 180 °C; (c) Compressive stress relaxation curves at 180 °C with an applied true stress of 205 MPa; (d) Relaxing stresses in 30 min at 180 °C with various applied stresses of 135 MPa, 175 MPa and 205 MPa; and (e) Compressive creep curves of the T4 and T6 alloys tested at 210 °C with100 MPa; (f) shows an enlarged portion of creep for first 20 hours in (e).

3.3 Microstructural characterization

Fig. 3 contains bright field TEM micrographs of the T4 and T6 alloys before and after stress relaxation and creep tests. In the T4 alloy (Fig. 3a), intermetallic compounds were absent within the grains and along the grain boundaries. But, low density dislocations can be observed, which were possibly resulted from the quenching process and/or the mechanical grinding during TEM sample preparation. In the T6 alloy, three types of precipitates with different morphologies were identified in the α-Mg grains. Fig. 3b is a TEM micrograph viewed along the $< 11\bar{2}0 >$ axis, in which the different precipitates could be observed as indicated by the labelled arrows. The Type 1 precipitates are block-shaped and highly likely formed on the $\{11\bar{2}0\}$ planes. The Type 2 precipitates are on the prismatic plane and in a rod shape. The Type 3 precipitates formed on the basal plane with a large aspect ratio, and were only sparsely distributed compared to Type 1 and Type 2 precipitates in the T6 alloy.

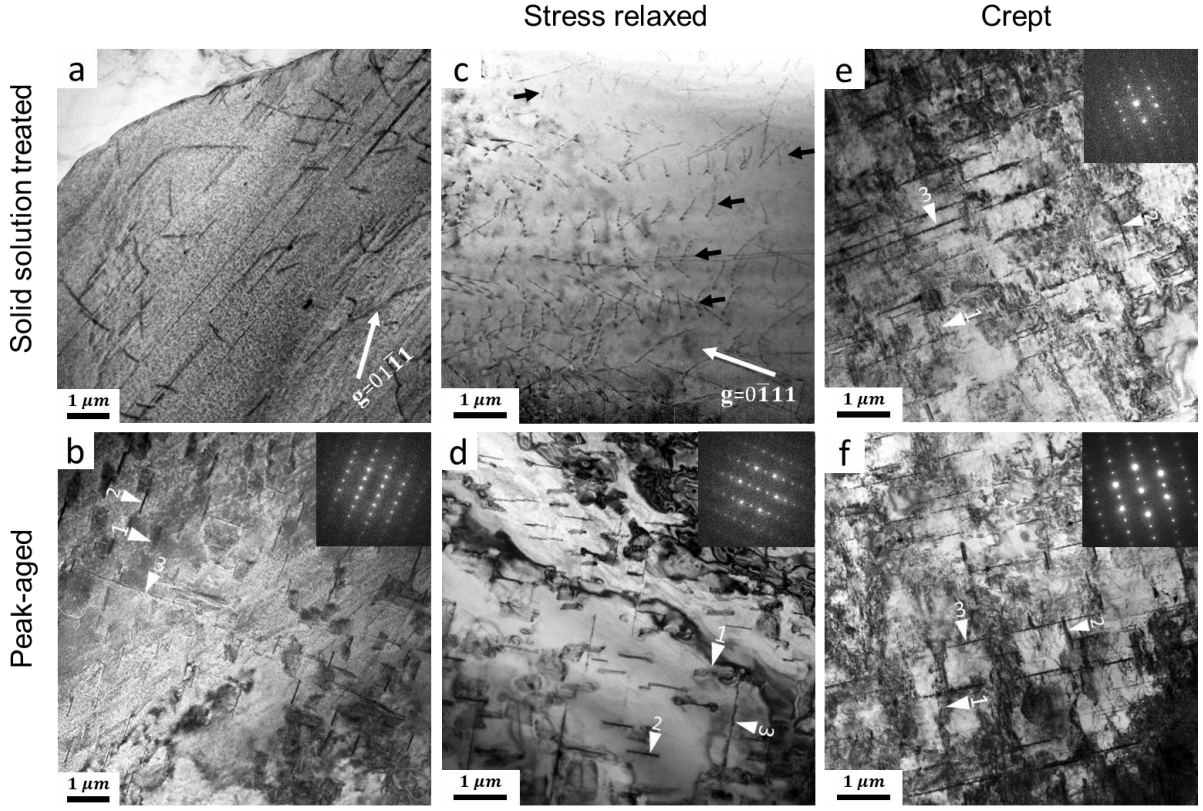

Figure 3 Transmission electron micrographs with the electron beam parallel to $< 11\bar{2}0 >_{Mg}$ direction, showing the typical microstructure of the Mg-0.5Gd-1.2Ca alloy. (a) as solution treated T4 alloy; (b) as peak-aged T6 alloy; (c) the T4 alloy after stress relaxation test at 205 MPa for 30 min; (d) the T6 alloy after stress relaxation test at 205 MPa for 30 min; (e) the T4 alloy after creep test at 210 °C for 100 h; and (f) the T6 alloy after creep test at 210 °C for 100 h

Typical microstructure of the two alloys after stress relaxation tests for 30 min at 180 °C with an applied stress of 205 MPa are shown in Figs. 3c and 3d. Due to the short time of 30 min precipitation did not occur and no precipitates were observed in the T4 alloy. But the compression resulted in the change in dislocation morphology. As shown in Fig. 3c, some

dislocations piled up in arrays as indicated by the black arrows. Dislocations in the arrays are parallel to each other. However, there is no evidence of the obstacles responsible for the piling up. In addition, the stress relaxation test did not significantly change the microstructure of the T6 alloy as shown in Fig. 2d. The three types of precipitates formed during ageing process were still observed.

After creep testing at 210 °C for 100 h, similar microstructures are observed in both the T4 and T6 alloys, as shown in Figs. 3e and 3f. Dynamical precipitation occurred in both alloys, leading to the formation of the three types of precipitates previously identified in the T6 alloy. In comparison with the microstructure prior to creep, crept alloys contained much more Type 3 basal precipitates. Type 1 block-shaped precipitates were slightly coarsened, but the size of the Type 2 and Type 3 precipitates was similar with those in the peak-aged T6 alloy. To quantitatively describe the morphology and fraction of the precipitates, the average lengths and the number density of each type of precipitate were measured based on TEM foil thickness using a CBED technique. Results for T6, crept T4 and crept T6 alloys are shown in Fig. 4. Quantitative data about the average size in Fig. 4a proved the above description that the Type 1 precipitates were coarsened after creep. And the number density of the precipitates in the crept T4 and T6 alloys is higher than the as peak aged T6 alloy. This implies that new precipitates, especially Type 3 precipitates, formed in alloys during creep testing. In comparison between the crept T4 alloy and the crept T6 alloy, the number density of all three types of precipitates in the crept T4 alloys was 15%-30% higher than those in the crept T6 alloy. As a result, the total number densities were estimated to be $6.1 \times 10^{18} m^{-3}$ and $3.8 \times 10^{18} m^{-3}$ in the crept T4 and T6 alloys, respectively.

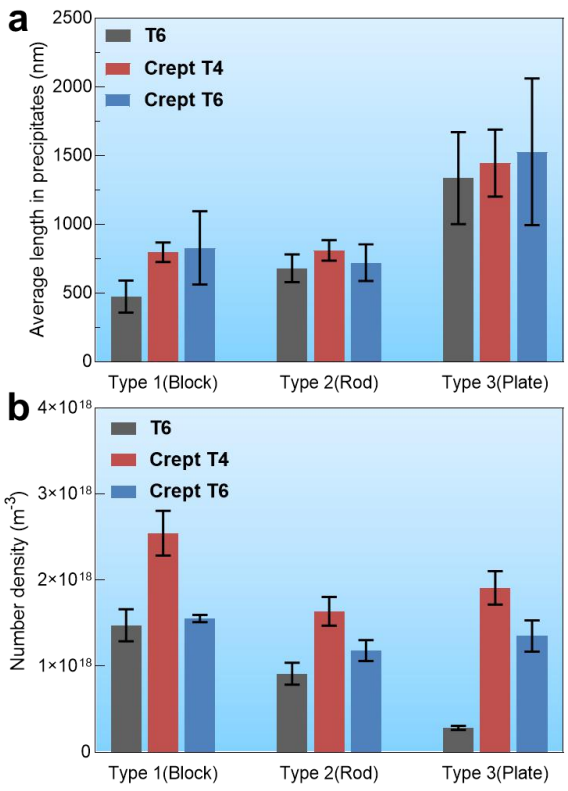

Figure 4 (a) Average lengths and (b) number density of precipitates measured in peak-aged (T6), crept T4 and crept T6 alloys

The Type 1 and Type 2 precipitates in both T4 and T6 alloys were further examined from different orientations. Fig. 5 are typical TEM micrographs and the corresponding diffraction patterns in the T4 alloy after creep for 100 hours. It was found that the Type 1 precipitates formed heterogeneously on pre-existing dislocations when examined along the [0001] axis (Fig. 5b). The selected area electron diffraction (SAED) patterns for this type of precipitates, taken along the $[01\bar{1}0]$ and [0001] axes (Figs. 5c and 5d), verified that the Type 1 precipitate was the Mg_2Ca phase. The orientation relationship between the Type 1 precipitate and the Mg matrix was $[01\bar{1}0]_{Mg} \parallel [12\bar{1}0]_{Mg_2Ca}$ and $(0001)_{Mg} \parallel (0001)_{Mg_2Ca}$, which is consistent with orientation relationships as previously reported [35]. The Type 2 prismatic precipitates were further identified as β phase, Mg_5Gd, by Fast Fourier Transform (FFT) patterns taken along the $[11\bar{2}0]$ and [0001] zone axes as shown in Figs. 5e and 5f. The orientation relationships with the Mg matrix are $[2\bar{1}\bar{1}0]_{Mg} \parallel [1\bar{1}1]_{\beta}$ and $(0001)_{Mg} \parallel (110)_{\beta}$, as previously published [36]. The same results were also obtained in the T6 alloy.

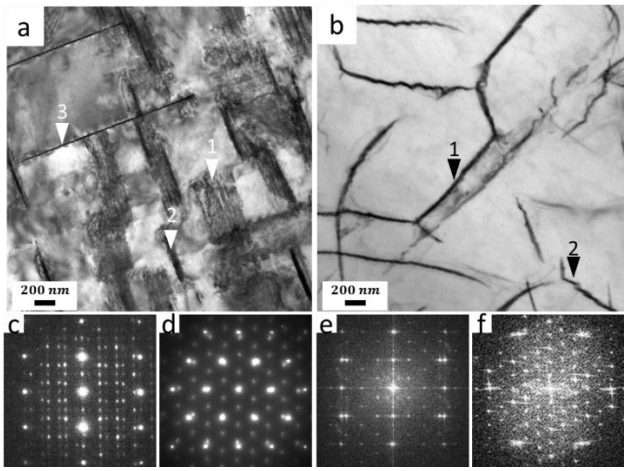

Figure 5 TEM micrographs and the corresponding electron diffractions in the T4 alloy after creep test at 210 °C for 100 h. (a) Bright filed image along $[11\bar{2}0]$ axis; (b) bright filed image along $[0001]$ axis; SAED pattern for Type 1 precipitate (Mg_2Ca) taken along (c) $[01\bar{1}0]$ direction and (d) $[0001]$ direction; FFT pattern for the Type 2 precipitate (Mg_5Gd) taken along $[11\bar{2}0]$ direction and (f) $[0001]$ direction.

TEM-EDX spot analysis was carried out on the thin basal precipitate to identify the Type 3 precipitate. Almost equal-atomic Gd and Ca content was detected in addition to Mg as shown in Figs. 6a and 6b. Figs. 6c-f are the HRTEM images and the corresponding FFT patterns for the basal precipitate taken along the $[2\bar{1}\bar{1}0]$ and $[10\bar{1}0]$ zone axes of the Mg matrix. The FFT patterns of this Mg-Gd-Ca basal precipitate were very similar to the unidentified precipitate recently reported in the work by Shi et al. [37]. HRTEM images indicated the thickness of this type of precipitate to be about 3-6 nm and fully coherent with the Mg matrix along the (0001) habit plane. However, this precipitate was invisible when viewed along the [0001] axis in the bright filed image, as shown in Fig. 4b, as well as in the HRTEM image. Thus, further investigation is required to actually identify the crystal structure of this type of precipitate formed on the basal plane.

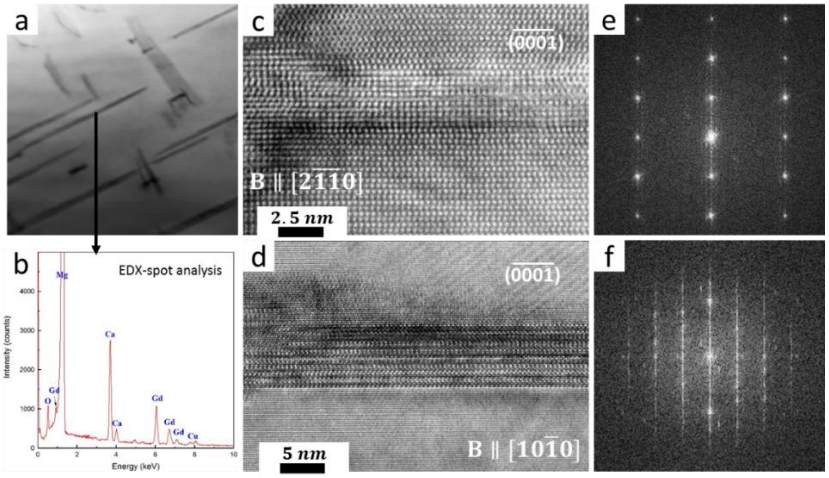

Figure 6 (a) Bright field STEM image and (b) EDX spot analysis of Type 3 basal precipitates in the T4 alloy after creep testing at 210 °C for 100 h; (c) HRTEM image along $[2\bar{1}\bar{1}0]$ direction; (d) HRTEM image along $[10\bar{1}0]$ direction; (e) FFT pattern of the Type 3 basal precipitate taken $[2\bar{1}\bar{1}0]$ direction; and (f) FFT pattern of the Type 3 basal precipitate taken $[10\bar{1}0]$ direction.

3.4 Solute distribution in the Mg-0.5Gd-1.2Ca alloy

Both the APT and HAADF-STEM were employed to investigate the architecture of solutes in the Mg-0.5Gd-1.2Ca alloy. In order to focus on the solute distribution in the solid solution, grain boundaries and precipitates were avoided when conducting APT analysis in both the T4 and T6 alloys. Fig. 7 shows a three-dimensional reconstruction of the area analysed in the as solid solution treated T4 alloy. The tomographic maps show a highly uniform elemental distribution of Gd and Ca solutes and the absence of any visible solute clusters within this specimen volume. The tomographic map for the α-Mg matrix (excluding the precipitates and grain boundaries) in the as peak-aged T6 alloy is the same and is therefore not shown. As the atom probe analysis is localized [38], EPMA spot analysis was used to show the average matrix compositional difference between the T4 and T6 alloy. The average concentrations determined using EPMA are listed in Table 1. The solid solution treated T4 alloy contained nearly equivalent contents of Gd and Ca solutes. The measured Gd content was close to the nominal value, but the Ca was determined to be less than half of the nominal value. The discrepancy was resulted from the low solubility of Ca in Mg, leaving more undissolved intermetallic compounds along grain boundaries after solid solution treatment, as shown in Fig. 1c. After peak ageing, the Gd and Ca contents in the α-Mg matrix of the T6 alloy were reduced as a result of precipitation, specifically, the amount of Ca solute decreased more significantly than that of Gd.

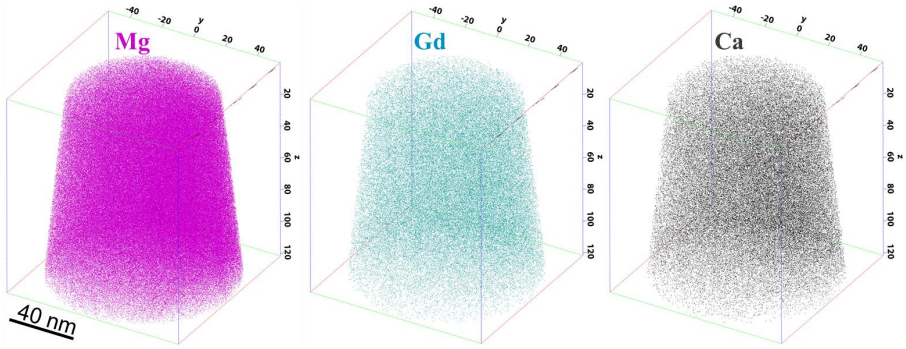

Figure 7 Tomographic maps showing the elemental distribution of Mg, Gd and Ca in the solid solution treated Mg-0.5Gd-1.2Ca alloy

The APT data obtained from both the T4 and T6 alloys were further analysed using a contingency table analysis. This is a statistical technique used to identify fine-scale co/anti-segregation effects of dilute micro-alloying solutes by comparing the observed frequencies of two elements with those expected for a random distribution. Table 2 shows the experimentally detected frequencies (n_{ij}) and estimated values (e_{ij}) for random Gd and Ca solute atoms based

on a block size of 100 atoms. The test of independence between statistically random and experimentally-observed distribution values were evaluated by a statistic, χ^2 [39, 40]:

$$\chi^2 = \sum_{i=1}^{r}\sum_{j=1}^{c}\frac{\left(n_{ij} - e_{ij}\right)^2}{e_{ij}} \quad (1)$$

where *r* and *c* are the number of rows and columns in each table, and (*r*-1) (*c*-1) is the degree of freedom. The calculated χ^2 value between Gd and Ca in the T4 alloy is 99.35 with 16 degrees of freedom, as shown in Table 2a, which is evidently bigger than the value (39.252) corresponding to a 0.001 probability of deviation greater than χ^2 (Appendix E of Ref. [39]). This indicates a low probability of a random distribution of Gd and Ca solute atoms. Instead, co-segregation of Gd and Ca are highly likely to be present in the solid solution. The T6 alloy had a lower calculated value of χ^2 (69.60) with 12 degrees of freedom. But, this χ^2 value is still higher than the value of 32.910 corresponding to a 0.001 probability of a deviation greater than χ^2, as shown in Table 2b. This suggests that the residual Gd and Ca solutes within the α-Mg matrix still tend to co-segregate but the tendency is not as high as it is in the solid solution treated T4 alloy.

Table 1 Elemental composition (at.%) of Mg-Gd-Ca alloy corresponding to EPMA spot analysis

Element	Actual (at.%)		Nominated (at.%)
	Solid solution (T4)	Peak-aged (T6)	
Mg	Bal.	Bal.	Bal.
Gd	0.42 ± 0.01	0.30 ± 0.03	0.5
Ca	0.37 ± 0.01	0.18 ± 0.05	1.2

In addition, a separate statistical methodology, namely generalized multicomponent short-range order (GM-SRO) [41-44], is utilised to further examine the distributions and interactions of Gd and Ca solute atoms within Mg solvent atoms. This statistical approach is based on the radial-distribution analysis, which is able to examine the local neighbourhood as a function of distance extending radially outwards from each atom. The GM-SRO concept is extended from the classic Warren-Cowley short-range order parameter (WC-SRO) [45] and pairwise multicomponent short-range order (PM-SRO) [46], but considers two sets of atomic species rather than just two individual atomic species for each parameter. In this way, the GM-SRO parameter α is defined as [41, 42]

$$\alpha^{m}_{\{B_j\}_{j=1}^{k}\{B_l\}_{l=0}^{h}} = (-1)^{\left(1+\delta_{\{B_j\}_{j=1}^{k}\{B_l\}_{l=0}^{h}}\right)} \frac{\left(p^{m}_{\{B_j\}_{j=1}^{k}\{B_l\}_{l=0}^{h}} - X_{\{B_l\}_{l=0}^{h}}\right)}{\left(\delta_{\{B_j\}_{j=1}^{k}\{B_l\}_{l=0}^{h}} - X_{\{B_l\}_{l=0}^{h}}\right)} \quad (2)$$

where $\delta_{\{B_j\}_{j=1}^{k}\{B_l\}_{l=0}^{h}}$ equals to one, when the two sets of atomic species are identical and zero otherwise; $X_{\{B_l\}_{l=0}^{h}}$ is the combined concentration of the neighbouring species, and $p^{m}_{\{B_j\}_{j=1}^{k}\{B_l\}_{l=0}^{h}}$ is the probability of finding particular types of atoms, B_j, around another atom of any species, B_l, in the mth shell. Hence, a positive value of α is indicative of co-segregation in that crystallographic cell, a negative value of α otherwise indicates anti-segregation between the two sets of atoms, and a value equal to zero demonstrates the random distribution.

Table 2 Contingency tables for Gd and Ca in the (a) as solid solution treated T4 alloy and (b) peak-aged T6 alloy.

a T4 alloy

	Gd						Gd				
Ca	0	1	2	3	4-100		0	1	2	3	4-100
(a) Experimental observations, n_{ij}						(b) Estimated values, e_{ij}					
0	91714	32575	6422	922	128	0	90929	33109	6627	961	134
1	36239	13671	2783	403	64	1	36686	13358	2674	388	54
2	7593	3025	648	103	8	2	7851	2859	572	83	12
3	1114	481	109	17	1	3	1188	433	87	13	12
4-100	150	63	9	1	1	4-100	155	56	11	2	0
$\chi^2 = 99.35 > \chi^2(0.001) = 39.252$ with 16 degrees of freedom											

b T6 alloy

	Gd						Gd				
Ca	0	1	2	3	4-100		0	1	2	3	4-100
(a) Experimental observations, n_{ij}						(b) Estimated values, e_{ij}					
0	104765	33070	6879	1143	204	0	104282	33322	7036	1199	222
1	22664	7572	1680	306	61	1	23049	7365	1555	265	49
2	2677	917	214	45	13	2	2760	882	186	32	6
3-100	235	90	21	4	0	3-100	250	80	17	3	1
$\chi^2 = 69.60 > \chi^2(0.001) = 32.910$ with 12 degrees of freedom											

The calculated GM-SRO parameters for both the solid solution treated T4 alloy and peak-aged T6 alloy are presented in Fig. 8 from the perspective of Mg, Gd and Ca atoms respectively. In the solid solution treated condition (Figs. 8a-c), Gd-Ca and Ca-Gd pairs displayed highly positive GM-SRO parameters and thus indicated a strong trend of Gd and Ca atoms to co-segregate together, which is consistent with the results from the contingency table analysis (Table 2). As Gd and Ca atoms co-segregate together, Mg atoms correspondingly anti-segregate with them in the solid solution and hence cases of Mg-Gd/Gd-Mg and Mg-

Ca/Ca-Mg exhibited negative parameters in the nearest 9 shells. In addition, curves of Mg-Gd/Gd-Mg and Mg-Ca/Ca-Mg presented with a similar pattern which was most strongly negative only in a short range of the nearest distance between the 2nd and the 5th shell, they then become more neutral in higher shells (>6th shell). Gd-Gd and Ca-Ca appeared to be random as their values were close to zero in all shells. Combined results hence indicated that Gd and Ca atoms tend to form short-range co-clusters in the Mg solid solutions. The peak-aged specimen showed a similar pattern of co- and anti-segregation for all sets of atomic species (Figs. 8d-f). The co-segregation of Gd and Ca in peak-aged specimen was also confirmed by the contingency table. However, it is necessary to note that within the peak-aged specimen, the interaction between matrix atoms (Mg) and solute atoms (Gd and Ca) became weaker as the negative sign of parameters for the set of Mg-Gd and Mg-Ca was lower than that of the solid solution specimen.

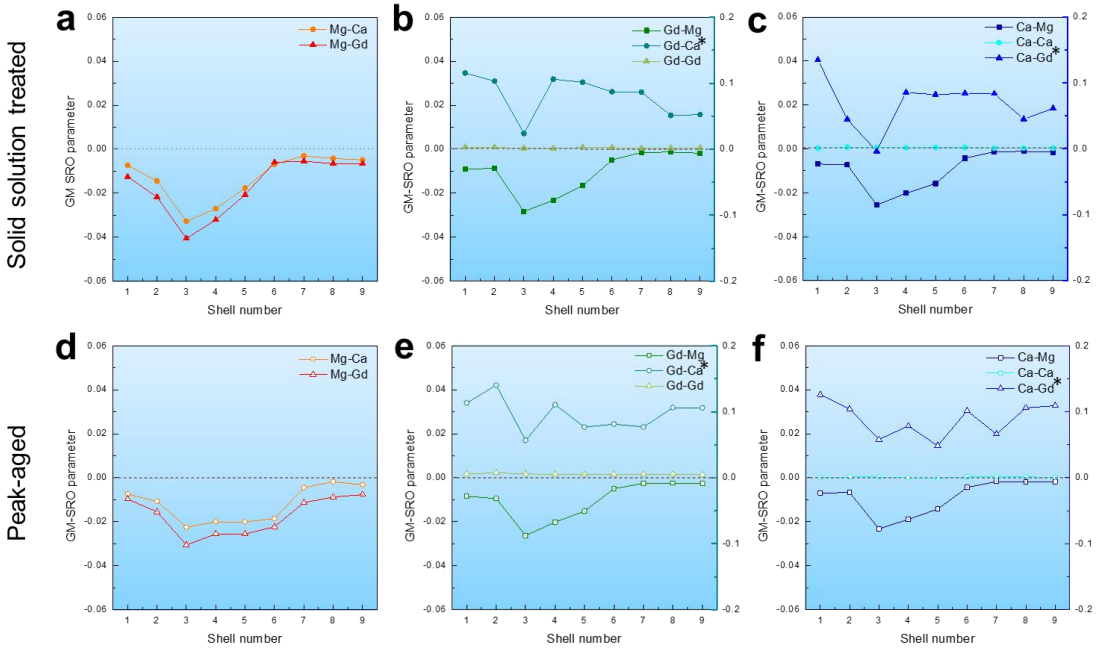

Figure 8 The calculated GM-SRO parameters in the first 9 nearest-neighbour shells calculated based on the experimental APT data for: (a-c): the as solid solution treated T4 alloy; and (d-f): the as peak-aged T6 alloy. The curve with superscript * was plotted with the right Y axis.

To further reveal and describe the detail of Gd-Ca co-clusters, HAADF-STEM was applied to the as solid solution treated T4 alloy. The images are shown in Fig. 9. Since the atomic numbers of Gd and Ca are higher than Mg, bright dots in the HAADF-STEM images represent a column rich in Gd/Ca solute atoms. The low-magnification image (Fig. 9a) reveals that triangular clusters comprising three Gd/Ca-rich atom columns were frequently observed in the α-Mg matrix of the T4 alloy as indicated by white arrows. Inspection of the triangular shaped clusters in Fig. 9b shows solute-rich columns were distributed at opposite corners of a

hexagon along the $< 10\bar{1}0 >_{Mg}$ direction. The distance between each two adjacent solute-rich columns in the cluster was determined to be 0.37 nm. Figs. 9c-n show the presence of other clusters, formed in the same manner but comprised of more than three solute-rich columns in both original format and filtered format. In comparison, the original format could provide with a real contrast for atom columns while filtered images showed a clearer arrangement of the clustering. Bright columns with different contrast can be observed as marked with numbers in original images (Fig. 9c-g). It can be observed that the columns labelled as #1 were apparently darker when compared to those columns labelled as #2 within the same solute cluster. Those features supported the evidence in APT that Gd and Ca were co-clustered together, resulting in different contrast owing to the difference in atomic number of Ca (20) and Gd (65). These clusters were clearly seen in filtered images (Fig. 9i-n) that able to be assembled by the triangle shaped clusters as a unit. Hexagonal shaped clusters were also detected, although only sparsely distributed, in the solid solution treated microstructure (Fig. 9n). More HAADF images describing this type of Gd-Ca co-cluster were refer to Fig. S1.

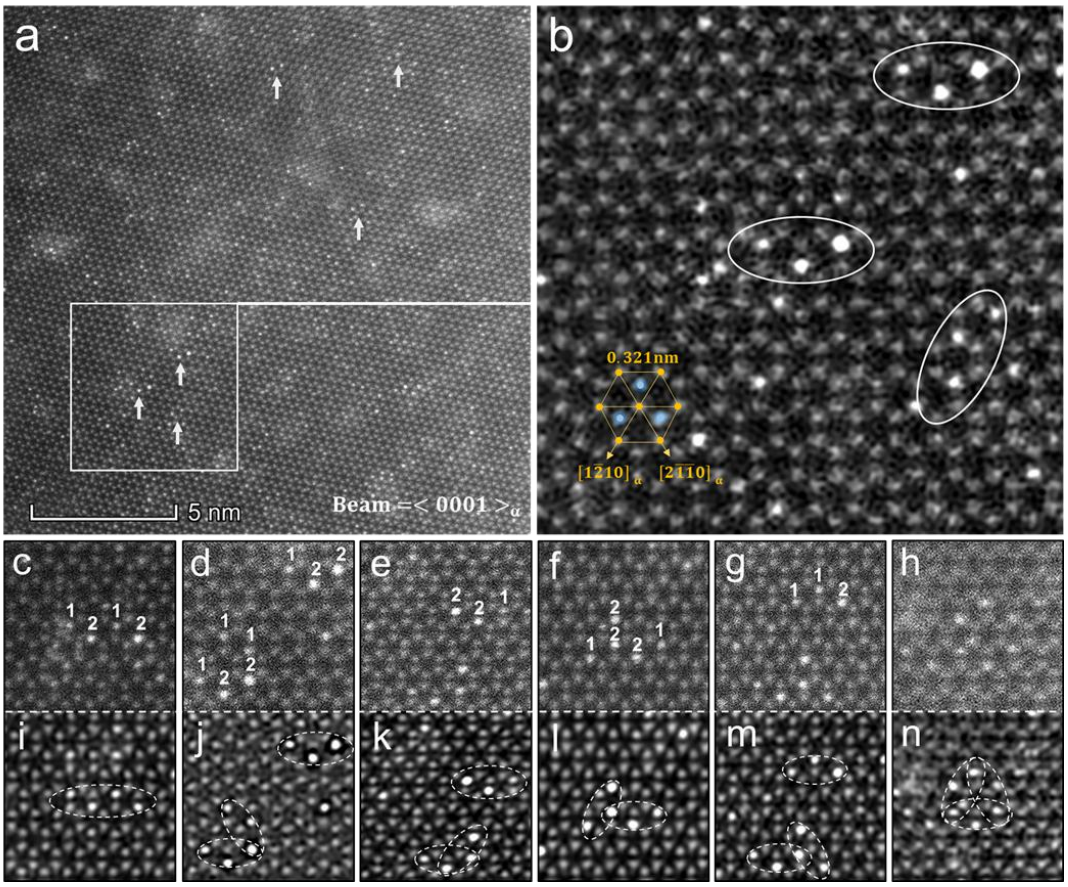

Figure 9 (a) HAADF-STEM image of the solute distribution within the α-Mg matrix of the solid solution treated T4 alloy; (b-h) Higher-magnification images showing the configuration of solute clusters in the alloy. Electron beam was parallel to $[0001]_{Mg}$.

3.5 Comparison of the Mg-0.5Gd-1.2Ca alloy with Mg-Al alloy in GM-SRO parameters

The APT analysis was also applied to an Mg-Al in order to compare the solute distribution in the Mg-0.5Gd-1.2Ca alloy with that in an alloy that is commonly known having low creep resistance [7, 47]. Fig. 10 shows the three-dimensional reconstructed tomographic image of the as solid solution treated Mg-Al specimen. Like the Mg-0.5Gd-1.2Ca alloy, Al solute and Mg solvent are seen to be evenly distributed within the α-Mg grains. No large-scale clusters formed in the solid solution treated Mg-Al alloy. The concentration of Al in the APT specimens were measured to be 3.68 at.%. Experimental GM-SRO parameters for the Mg-Al alloy are compared with the solid solution treated Mg-Gd-Ca alloy in Fig. 11. Similar to the T4 and T6 alloys as shown in Fig. 8, the GM-SRO parameter for the Al-Mg and (Gd, Ca)-Mg pairs is negative, the Al-Al pair is zero and the Gd-Ca pair is positive. It can be seen that Al atoms slightly co-segregated in the specimen as the Al-Al parameter was positive in the first several shells. Correspondingly, Mg and Al atoms were anti-segregating in the solid solutions and were negative for the Mg-Al/Al-Mg pairs. However, the GM-SRO parameters in the Mg-Al solid solution were more moderate when compared with the Mg-Gd-Ca solid solution, even if the Al concentration (3.68 at.%) was almost ten times higher than the concentration of Gd (0.42 at.%) and Ca (0.37 at.%).

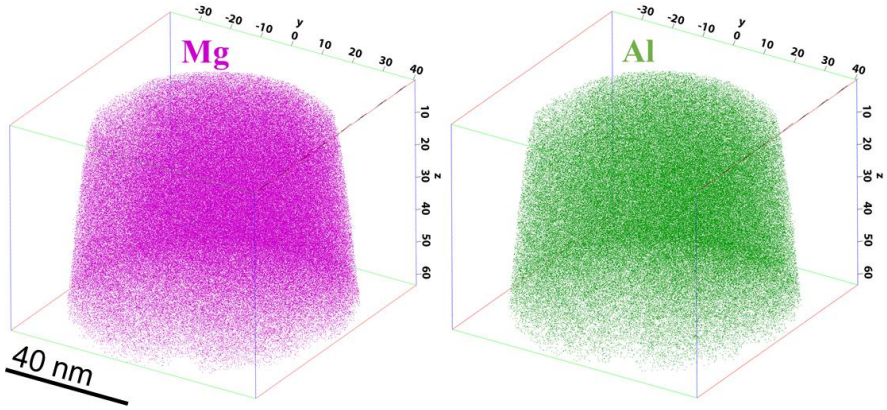

Figure 10 Tomographic maps showing the elemental distribution of Mg and Al in the solid solution treated Mg-Al alloy.

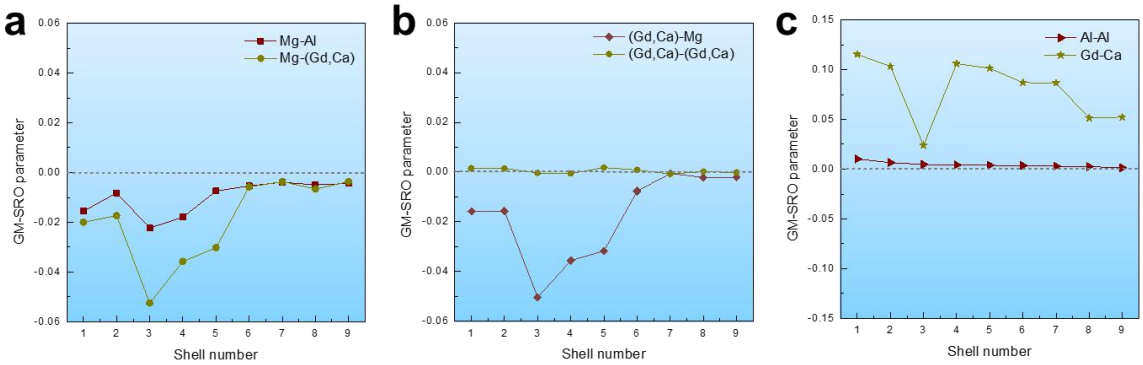

Figure 11 The calculated GM-SRO parameter in first 9 nearest-neighbour shells based on the experimental APT data for the as solid solution treated Mg-Al alloy in comparison with the as solid solution treated T4 alloy.

4. Discussion

4.1 Strengths and stress relaxation resistance of the Mg-0.5Gd-1.2Ca alloy

For magnesium alloys, solid solution strengthening and precipitation strengthening are considered as the predominate mechanisms enhancing mechanical performance [6]. Thus, this work reports the effect of solid solution and aging treatment on mechanical properties of the newly-developed Mg-0.5Gd-1.2Ca (at.%) alloy. As shown in Fig. 2a, the T6 alloy showed higher room temperature compression than the T4 and the as-cast alloys. Obviously, the precipitation strengthening was responsible for the strength enhancement. However, when the compression was done at 180 °C, both yield strength and ultimate strength of the T6 alloy were reduced significantly by more than 40 MPa, whereas strengths of the T4 alloy remained almost the same as room temperature (Figs. 2a-b). Furthermore, the T4 alloy also had higher stress relaxation resistance than the T6 alloy at 180 °C (Fig. 2c). The better mechanical performance of the T4 alloy at elevated temperature could be attributed to either solid solution strengthening or dynamic precipitation strengthening or both. But, Fig. 3c shows no occurrence of dynamic precipitation with 30 minutes stress relaxation but the rearrangement of dislocations. Considering that compression test was even less than 30 minutes, dynamic precipitation was unlike to occur, it seems that the solid solution strengthening governed the better performance of the T4 alloy at elevated temperatures.

Similar mechanical behaviours were also reported in other low-RE Mg alloys. Gravas et al. [15] reported that although the peak-aging effectively improved tensile strengths of the Mg-0.45La-1.18Y (at.%) alloy at room temperature, the solid solution treated alloy exhibited lower creep strain than the peak-aged alloy tested at 177 °C for 600 h. In this work, no dynamic precipitates were detected in the solid solution treated alloy after creeping. Combined with the present results, it should be reasonable to conclude that solid solution strengthening is more effective to resist the high temperature softening of the low-RE Mg-alloys, even though concentrated Mg-RE based alloys showed better high-temperature properties at peak-aging condition [48, 49]. The questions remained are: (1) why did such phenomenon only occur in low-RE Mg alloys; (2) why was the solid solution strengthening more effective at elevated temperature; (3) what was the actual cause of the higher efficiency of solid solution strengthening of REs and Ca at elevated temperature than other solutes, such as Al and Zn. In addition, it needs to be noted that solid solution strengthening is not stable at elevated temperatures because the supersaturation of solutes tends to be reduced through

precipitation. To answer these questions, microstructure obtained is further discussed as follows.

4.2 Precipitates in the T6 alloy and Gd-Ca co-clusters in the T4 alloy

As shown in Fig. 1, intermetallic compounds formed in the interdendritic regions in the as-cast alloy. Even after solid solution treatment, a small fraction of undissolved intermetallic phases still remained along grain boundaries. Grain boundary reinforcement by these intermetallic compounds were verified as the least important factor contributing to the high-temperature properties because the as-cast alloy exhibited much lower strength and stress relaxation resistance than the peak-aged and solid solution treated alloys. Thus, the contribution of undissolved intermetallic phases in both the T4 alloy (Fig.1c) and the T6 alloy (Fig.1d) can be neglected.

TEM examination indicated that the age hardening effect in the T6 alloy was attributed to the Type 1 Mg_2Ca precipitates and the Type 2 prismatic β Mg_5Gd precipitates as shown in Fig. 3b. The sparse distribution of the Type 3 Mg-Gd-Ca basal precipitates however is expected to provide only a marginal effect. Two reasons could be accounted for the presence of the equilibrium β Mg_5Gd precipitate rather than the metastable β' and β_1 in the peak-aged microstructure of the present alloy. One is due to the low Gd concentration. P. Vostrý et al. [23] reported that the precipitation of metastable phase was absent during aging process of the Mg-4.47Gd and Mg-9.33Gd (wt.%) alloys, and the stable β phase was responsible for the aging response of these alloys. The formation of β Mg_5Gd phase has also been reported in other of low-Gd containing alloys, such as the Mg-4.5Zn-1.5Gd (wt.%) [50] and the Mg-6Gd-0.6Zr (wt.%) alloys [22]. The second reason is related to Ca. A recent work by Chen et al. [51] indicated that Ca addition in a Mg-15Gd-0.6Ca-0.5Zr (wt.%) alloy was segregated into β_1 and β (Mg_5Gd) precipitate, and it was considered that Ca reduced the nucleation barrier and promoted the precipitation of Mg_5Gd phase. It is therefore conceivable that the formation of β Mg_5Gd precipitates in this peak-aged alloy was owing to the low concentration of Gd and the acceleration effect of Ca addition on Mg_5Gd precipitate. Nevertheless, those precipitates formed in the T6 alloy provided effective precipitation strengthening, increasing both yield strength and ultimate compressive strength at room temperature, as shown in Fig. 2a. However, at 180 °C, the precipitation strengthening effect was evidently weakened despite no visible coarsening of or morphological change to the precipitates in the aged alloy after compression (Fig. 3d). In contrast, the T4 alloy exhibited more stable strengths

and lower stress relaxation at elevated temperatures (Fig. 2b-c). The absence of dynamic or strain-induced precipitation in the T4 alloy after stress relaxation (Fig.3c), implies that better mechanical performance can be totally attributed to solid solution strengthening, which is consider as the result of Gd-Ca co-clusters.

As shown in Fig. 7, although the atom probe tomographic maps seem to exhibit a random distribution of Gd and Ca solutes in Mg matrix (Fig. 7), further statistical analysis by the contingency table and GM-SRO program indicate that the Gd and Ca atom distributions throughout the Mg solid solution have in fact significantly deviated from the random distribution. Contingency table is a well-established statistic method that have been widely used in magnesium alloys to identify fine-scale features [52-54]. The results of the contingency table shown in Table 2 verifies that co-segregation of Gd and Ca atoms occurred in the supersaturated solid solution of magnesium in the as solid solution treated T4 alloy. Assessment by the recently developed GM-SRO program provides with a straightforward view that Gd and Ca atoms tend to form co-clusters within a short-range of the Mg solid solution (Fig. 8). These Gd-Ca co-clusters are further identified by HAADF-STEM to have a strong preference to form in a triangular shape and/or other structures extend from this triangular-shaped cluster as shown in Fig. 9. Similar configurations of cluster have previously been detected in Mg-RE (including Gd) binary alloys at the early aging stage and are generally referred to as short-range order structure [55-60]. But the presence of clusters with similar short-range order in the as-solid solution treated Mg-REs based alloy is reported for the first time in the present work. A distinction is that those clusters in pre-aged binary Mg-Gd alloys were extensively formed in six-column hexagonal and zig-zag shapes rather than the three-column triangular shape as observed in the current study [55, 58, 59]. As pointed out by Nie et al. [60], the formation of favourable shapes of RE clusters is controlled by minimization of the elastic strain associated with individual solute atoms based on first principle calculations. As the measured atomic radius for Gd and Ca are both 0.180 [61], it is reasonable to propose that the formation of Gd and Ca co-clusters with similar shapes to the binary Mg-RE alloys, is also driven by minimization of the elastic strain of single Gd and Ca atoms, where some Gd atoms are replaced by Ca atoms, as shown in Fig. 12a.

Starink et al. [62] indicated that strengthening mechanisms of co-clustering in metallic alloys, including the (short-range) order strengthening effect, has led to the examination of order strengthening as the main strengthening mechanism of co-clusters in a wide range of Al-Cu-Mg alloys. Hence, it is expected that Gd-Ca co-clusters, exhibiting short-range order structure in the supersaturated solid solution of the Mg-0.5Gd-1.2Ca (at.%) alloy, offered a

strong local order strengthening effect in addition to the atomic and modulus mismatch hardening. According to the classic theory by Fisher [63, 64], the local order strengthening mechanism suggests that passing dislocations destroy the local order and produces more random configurations with higher energy. The extra stress increment, caused by the destruction of local order, is required to maintain the displacement of such dislocations, which is not determined by a thermal activation process at a range of temperatures below the point that self-diffusion happens [63, 64]. Thus, the local order strengthening in solid solution provides an athermal forest hardening effect and extends the athermal strength regime as shown in Fig. 12b [65]. Owing to the local order effect, Gd-Ca co-clusters in the T4 alloy subsequently lift the athermal regime, resulting in more thermally-stable strengths and better stress relaxation and creep resistance at elevated temperatures. However, for the T6 alloy, precipitation strengthening is normally weakened as temperature increases due to the higher mobility of dislocations. Furthermore, ageing enabled the formation of precipitates, reducing the concentration of the solutes. Some solutes still remain in the Mg solid solution and form co-clusters, as indicated by the contingency table (Table 2) and the GM-SRO (Fig. 8d-f), but, due to the low solute concentration, the number of such clusters in the T6 alloy would be lower than the T4 alloy, which was associated with a weaker order strengthening effect. As a consequence, the peak-aged T6 alloy experienced a higher softening effect on the compression strength and stress relaxation resistance at elevated temperatures in spite of the additional precipitation strengthening effect.

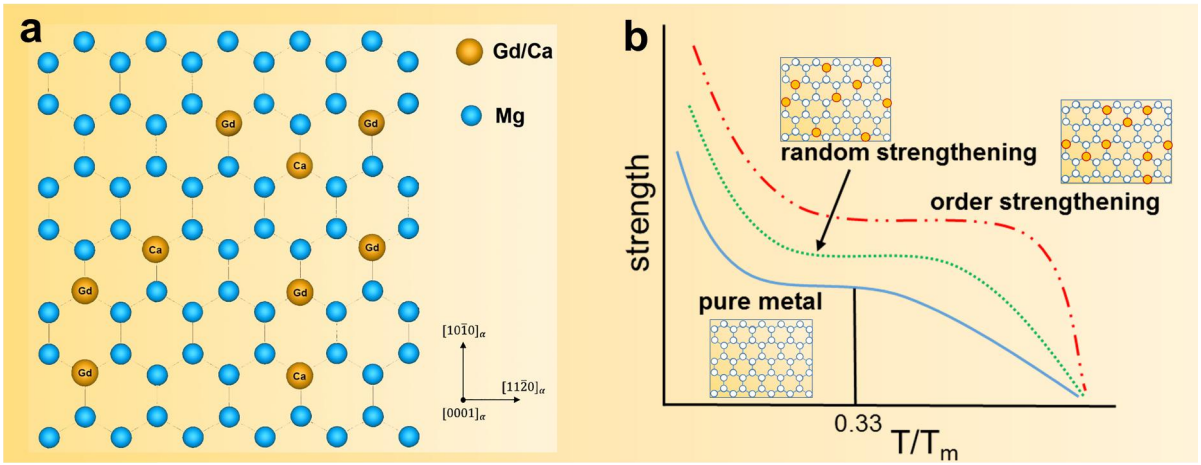

Figure 12 Schematic diagram showing (a) the short-range co-clusters comprised of Gd and Ca atoms in the the α-Mg matrix; (b) the solute hardening effect on the athermal regime [65].

The characteristics of the dislocation pile-ups (dislocation arrays), also called planar slip, as indicated by black arrows in Fig. 3c, is also evidence to support the existence of short-range order (SRO)/short-range cluster (SRC) in solid solutions, as widely reported [66-71].

Although similar dislocation pile-up could possibly be caused by the presence of obstacles or the formation of low-angle tilt boundaries in grains, these possibilities can be ruled out because dislocation arrays are seen to be closely parallel to each other and formed in the region without evident obstacles. This feature results from the movement of dislocations in a particular slip direction, which destroy the order of the SROs/SRCs across the plane, and therefore facilitates the gliding of successive dislocations on the same plane [63, 64, 68]. The same substructure of dislocations was also observed by Suzuki et al. [72] in an Mg-0.9Y-0.04Zn (at.%) solid solution alloy after high-temperature creep tests, even though the author claimed that it was on account of the low stacking fault energy (SFE). Work by Gerold et al. [67] suggested that SRO is the most important factor for the formation of this planar dislocation structure and that stacking fault energy is only one of the contributing factors.

4.3 Lower solid solution hardening effect in Mg-Al alloy

To answer the question why the better high temperature property occurred in RE/Ca-containing Mg alloys, the solid solution strengthening of other Mg alloys will be compared. Mg-Al based alloys, such as the AZ series, are widely used. However, the solid solution strengthening of Al to high-temperature strength and creep resistance is significantly lower than that of RE elements in magnesium. As mentioned in the introduction, the steady-state creep rate of the Mg-3Al (at.%) solid solution was one order of magnitude higher than that of the Mg-0.2Y (at.%) alloy [14]. The GM-SRO values shown in Fig. 11 indicate that Al solute tends to be distributed within the solid solution of Mg in a more random manner despite the Al concentration (3.68 at.%) being much higher. It has been identified by Absapour et al. [19, 20] that the athermal strength regime in the strength-temperature relationship for the AZ91 solid solution was limited to about 100 °C, whereas it was up to 250 °C for both Mg-0.8Gd (at.%) and Mg-0.9Ca (at.%) solid solutions. Therefore, the absence of a strong tendency to form fine-scale clusters offering order strengthening was responsible for the weaker solid solution strengthening of Al solute in Mg alloys at elevated temperatures.

4.4 Creep resistance of the Mg-0.5Gd-1.2Ca cast alloy

Although the solid solution strengthening by the Gd-Ca co-clusters showed higher efficiency at elevated temperatures in the T4 alloy that contained dilute Gd and Ca, in RE concentrated Mg alloys, precipitation strengthening still predominated the strengthening of the alloy resulted from the formation of large amount of precipitates. In addition, solid solution strengthening is also not stable at high temperature because precipitation will

eventually occur, reducing its effect. As shown in Fig. 2f, at very early stage of the creep test (within 30 minutes), the creep behaviours of both the T6 and T4 alloys were similar. Obviously, for the T6 alloy, the precipitation strengthening contributed to the creep resistance, and for the T4 alloy, it was the solid solution strengthening, the cluster effect in particular, resisting the creep. However, continuing creeping, even still within the primary stage, the T4 alloy showed better creep resistance than the T6 alloy. Because the primary stage creep of metals is dominated by hardening processes, including both solid solution and precipitation strengthening [73], the different creep behaviours of the T6 and T4 alloy were related to the change of key strengthening mechanisms. As both the grain size of the T6 and T4 alloys was almost the same (ageing at 180 °C did not significantly coarsen the grains), the creep strain resulted from the grain boundary gliding would not make the difference in both alloys. However, as shown in Figs. 3 b and f, it can be seen that the Type 1 precipitates in the T6 alloy were coarsened after creep test at 210 °C for 100 hours. This could lead to slightly over-ageing effect, reducing the resistance of the T6 alloy to creep. More importantly, from Fig. 4, it can be noticed that the number densities of the precipitates in the crept T4 alloy were higher than that of the crept T6 alloy even though sizes of precipitates were similar. Recent work on Al-Li-S4 alloy [74] and an extruded Mg-6Gd-1Ca alloy [75] verified that stress-induced dislocations during creep could act as nucleation sites for precipitates promoting the precipitation hardening response in comparison with isothermal aging. Hence, dynamic precipitation in the T4 alloy during creep led to formation of higher density of precipitates, which contributed to the resistance to creep strain. Hence it is reasonable to conclude that the dynamic precipitation in the T4 alloy during creep was responsible for the better creep resistance at later stage of the creep even though the solid solution strengthening was more predominated at early stage.

5. Conclusion

The strength and creep behaviour of a newly developed Mg-0.5Gd-1.2Ca (at.%) alloy under solid solution treatment and peak aged treatment have been investigated. The effect of Gd and Ca solutes on the high temperature mechanical properties have been clarified. The following conclusions can be drawn.

(1) Although peak aging (T6) effectively increased the room temperature compression strengths of the Mg-0.5Gd-1.2Ca (at.%) alloy, the as solid solution treated alloy (T4) exhibited higher strengths, stress relaxation resistance and creep resistance at elevated temperatures.

(2) After peak aging of the Mg-0.5Gd-1.2Ca (at.%) alloy, three types of precipitates, Mg_5Gd, Mg_2Ca and the basal Mg-Gd-Ca precipitates, were observed. The first two were responsible for the precipitation strengthening at room temperature. The basal Mg-Gd-Ca precipitates were dynamically induced during creep.

(3) Gd and Ca solutes in the α-Mg solid solution were verified having strong preference to form co-clusters by the combined effort of APT and HAADF-STEM. This co-cluster is expected to provide an additional local order strengthening contributing to the higher compression strength and stress relaxation resistance in the solid solution treated (T4) alloy at elevated temperatures.

(4) The APT analysis on a more concentrated alloy, Mg-3.68Al (at.%), indicated that Al atoms distributed in α-Mg matrix in a more random manner, corresponding to the poor strengthening effect of Al solutes on the creep behaviour of the Mg alloys.

(5) The as solid solution treated Mg-0.5Gd-1.2Ca (at.%) alloy (T4) showed better creep resistance than the peak aged alloy (T6) when tested at 210 °C/100 MPa for 100 hours. Microstructural analysis revealed that this is attributed to the synergistical effects of solid solution strengthening by the Gd-Ca co-clusters (particularly at early stage of creep) and dynamic precipitation hardening (particularly at the late stage of creep).

6. Acknowledgement

The authors acknowledge the facilities, and the scientific and technical assistance, of Microscopy Australia at the Australian Centre for Microscopy & Microanalysis (ACMM), The University of Sydney (Sydney Microscopy & Microanalysis). Part of the atom probe analysis was performed on the Atom Probe Workbench of the Characterisation Virtual Laboratory. NM, QT, MB and MXZ would also like to acknowledge to support of the School of Mechanical and Mining Engineering, University of Queensland and the Queensland Centre for Advanced Materials Processing and Manufacturing

7. Reference

[1] A. Luo, M.O. Pekguleryuz, Cast magnesium alloys for elevated temperature applications, J. Mater. Sci. 29 (20) (1994) 5259-5271.

[2] A.A. Luo, Recent magnesium alloy development for elevated temperature applications, Int. Mater. Rev. 49 (1) (2004) 13-30.
[3] B.L. Mordike, Creep-resistant magnesium alloys, Mater. Sci. Eng. A 324 (1–2) (2002) 103-112.
[4] M.O. Pekguleryuz, M. Celikin, Creep resistance in magnesium alloys, Int. Mater. Rev. 55 (4) (2010) 197-217.
[5] S.M. Zhu, M. Gibson, M. Easton, Z.S, Zhen, T. Abbott, Creep resistant magnesium alloys and their properties, MCT 58 (2) (2012).
[6] A.A. Luo, Materials comparison and potential applications of magnesium in automobiles, Essential Readings in Magnesium Technology, Springer, Cham, (2016) 25-34.
[7] N. Mo, Q. Tan, M. Bermingham, Y. Huang, H. Dieringa, N. Hort, M.X. Zhang, Current development of creep-resistant magnesium cast alloys: A review, Mater. Des. 155 (2018) 422-442.
[8] J.G. Wang, L.M. Hsiung, T.G. Nieh, M. Mabuchi, Creep of a heat treated Mg–4Y–3RE alloy, Mater. Sci. Eng. A 315 (1) (2001) 81-88.
[9] G. Riontino, D. Lussana, M. Massazza, G. Barucca, P. Mengucci, R. Ferragut, Structure evolution of EV31 Mg alloy, J. Alloys Compd. 463 (1) (2008) 200-206.
[10] S.M. He, X.Q. Zeng, L.M. Peng, X. Gao, J.F. Nie, W.J. Ding, Precipitation in a Mg–10Gd–3Y–0.4 Zr (wt.%) alloy during isothermal ageing at 250 C, J. Alloys Compd. 421 (1) (2006) 309-313.
[11] M. Easton, M.A. Gibson, S. Zhu, T. Abbott, J.F. Nie, C.J. Bettles, G. Savage, Development of magnesium-rare earth die-casting alloys, TMS (2018) 329-336.
[12] P. Vostrý, B. Smola, I. Stulikova, F. Von Buch, B.L. Mordike, Microstructure evolution in isochronally heat treated Mg–Gd alloys, Phys. Status Solidi A 175 (2) (1999) 491-500.
[13] J.F. Nie, Precipitation and hardening in magnesium alloys, Metall. Mater. Trans. A 43 (11) (2012) 3891-3939.
[14] M. Suzuki, H. Sato, K. Maruyama, H. Oikawa, Creep behavior and deformation microstructures of Mg–Y alloys at 550 K, Mater. Sci. Eng. A 252 (2) (1998) 248-255.
[15] S. Gavras, S.M. Zhu, J.F. Nie, M.A. Gibson, M.A. Easton, On the microstructural factors affecting creep resistance of die-cast Mg–La-rare earth (Nd, Y or Gd) alloys, Mater. Sci. Eng. A 675 (2016) 65-75.
[16] K. Maruyama, M. Suzuki, H. Sato, Creep strength of magnesium-based alloys, Metall. Mater. Trans. A 33 (13) (2002) 875-882.
[17] L. Gao, R.S. Chen, E.H. Han, Solid solution strengthening behaviors in binary Mg-Y single phase alloys, J. Alloys Compd. 472 (1) (2009) 234-240.

[18] L. Gao, R.S. Chen, E.H. Han, Effects of rare-earth elements Gd and Y on the solid solution strengthening of Mg alloys, J. Alloys Compd. 481 (1) (2009) 379-384.
[19] S. Abaspour, C.H. Cáceres, High temperature strength and stress relaxation behavior of dilute binary Mg alloys, Metall. Mater. Trans. A 47 (3) (2016) 1313-1321.
[20] S. Abaspour, V. Zambelli, M. Dargusch, C.H. Cáceres, Atomic size and local order effects on the high temperature strength of binary Mg alloys, Mater. Sci. Eng. A 673 (2016) 114-121.
[21] N. Mo, Q. Tan, B. Jiang, F. Pan, M.X. Zhang, Stress-relaxation behavior of magnesium-3gadolinium-2calcium-based alloys at elevated temperatures, Metall. Mater. Trans. A 48 (11) (2017) 5710-5716.
[22] J.F. Nie, X. Gao, S.M. Zhu, Enhanced age hardening response and creep resistance of Mg–Gd alloys containing Zn, Scripta Mater. 53 (9) (2005) 1049-1053.
[23] P. Vostrý, I. Stulikova, B. Smola, W. Riehemann, B.L. Mordike, Structure and stability of microcrystalline Mg-Ca alloy, Mater. Sci. Eng. A 137 (1991) 87-92.
[24] Y.Wang, G. Liu, Z. Fan, Microstructural evolution of rheo-diecast AZ91D magnesium alloy during heat treatment, Acta Mater. 54 (3) (2006) 689-699.
[25] K.B. Nie, K. Wu, M.Y. Zheng, X.S. Hu, X.J. Wang, Effect of ultrasonic vibration and solution heat treatment on microstructures and tensile properties of AZ91 alloy, 528 (2011) 7484-7487.
[26] P.M. Kelly, Quantitative electron microscopy, Met. Forum 5 (1982) 13-23.
[27] E.E. Underwood, The mathematical foundations of quantitative stereology, Stereology and quantitative metallography, ASTM International, 1972.
[28] B. Gault, M.P. Moody, J.M. Cairney, S.P. Ringer, Atom probe microscopy, Springer Science & Business Media, 2012.
[29] https://www.massive.org.au/cvl/cvl-workbenches/atom-probe-workbench (Last accessed in October 2018).
[30] S.M. Zhu, J.F. Nie, Serrated flow and tensile properties of a Mg–Y–Nd alloy, Scr. Mater., 50 (2004) 51-55.
[31] D.E. Fraser, P.A. Ross-Ross, A.R. Causey, The relation between stress-relaxation and creep for some zirconium alloys during neutron irradiation, J. Nucl. Mater. 46 (1973) 281-292.
[32] J.K. Solberg, H. Thon, Stress relaxation and creep of some aluminium alloys, Mater. Sci. Eng. A 75 (1985) 105-116.

[33] H. Gjestland, G. Nussbaum, G. Regazzoni, O. Lohne, Ø.Bauger, Stress-relaxation and creep behaviour of some rapidly solidified magnesium alloys, Mater. Sci. Eng. A 134 (1991) 1197-1200.

[34] H. Wang, B. Clausen, C.N.Tomé, P.D. Wu, Studying the effect of stress relaxation and creep on lattice strain evolution of strainless steel under tension, Acta Mater. 61 (4) (2013) 1179-1188.

[35] J.C. Oh, T. Ohkubo, T. Mukai, K. Hono, TEM and 3DAP characterization of an age-hardened Mg–Ca–Zn alloy, Scr. Mater., 53 (6) (2005) 675-679.

[36] X. Gao, S.M. He, X.Q. Zeng, L.M. Peng, W.J. Ding, J.F. Nie, Microstructure evolution in a Mg–15Gd–0.5 Zr (wt.%) alloy during isothermal aging at 250 C, Mater. Sci. Eng. A 431 (1-2) 2006) 322-327.

[37] L.L. Shi, Y. Huang, L. Yang, F. Feyerabend, C. Mendis, R. Willumeit, K.U. Kainer, N. Hort, Mechanical properties and corrosion behavior of Mg–Gd–Ca–Zr alloys for medical applications, J. Mech. Behav. Biomed. Mater. 47 (2015) 38-48.

[38] T. Homma, S. Nakawaki, K. Oh-ishi, K. Hono, S. Kamado, Unexpected influence of Mn addition on the creep properties of a cast Mg-2Al-2Ca (mass%) alloy, Acta Mater. 59 (2011) 7662-7672.

[39] M.K. Miller, Atom probe tomography analysis at the atomic level, New York: Kluwer Academic/Plenum Publishers; 2000.

[40] M.P. Moody, L.T. Stephenson, P.V. Liddicoat, S.P. Ringer, Contingency table techniques for three dimensional atom probe tomography, Microsc. Res. Tech. 70 (3) (2007) 258-268.

[41] A.V. Ceguerra, R.C. Powles, M.P. Moody, S.P. Ringer, Quantitative description of atomic architecture in solid solutions: a generalized theory for multicomponent short-range order, Phys. Rev. B 82 (13) (2010) 132201.

[42] A.V. Ceguerra, M.P. Moody, R.C. Powles, T.C. Petersen, R.K. Marceau, S.P. Ringer, Short-range order in multicomponent materials, Acta Crystallogr. A 68 (5) (2012) 547-560.

[43] B. Gault, M.P. Moody, J.M. Cairney, S.P. Ringer, Atom probe crystallography, Mater. Today 15 (9) (2012) 378-386.

[44] Y. Qiu, Y.J. Hu, A. Taylor, M.J. Styles, R.K.W. Marceau, A.V. Ceguerra, M.A. Gibson, Z.K. Liu, H.L. Fraser, N. Birbilis, A lightweight single-phase AlTiVCr compositionally complex alloy, Acta Mater. 123 (2017) 115-124.

[45] J.M.Cowley, An approximate theory of order in alloys, Phys. Rev. 77 (5) (1950) 669-675.

[46] D. de Fontaine, The number of independent pair-correlation functions in multicomponent systems, J. Appl. Crystallogr. 4 (1) (1971) 15-19.

[47] H. Somekawa, K. Hirai, H. Watanabe, Y. Takigawa, K. Higashi., Dislocation creep behavior in Mg–Al–Zn alloys, Mater. Sci. Eng. A 407 (1-2) (2005) 53-61.
[48] Y.H. Kang, X.X. Wang, N. Zhang, H. Yan, R.S. Chen, Effect of initial temper on the creep behavior of precipitation-hardenaed WE43 alloy, Mater. Sci. Eng. A 689 (2017) 410-426.
[49] J. Wang, L. Luo, Q. Huo, Y. Shi, Z. Xiao, Y. Ye, X. Yang, Creep behaviors of a highly concentrated Mg-18 wt% Gd binary alloy with and without artifical aging, J. Alloys Compd. 774 (2019) 1036-1045.
[50] J. Yang, W. Xiao, L. Wang, Y. Wu, L. Wang, H. Zhang, Influences of Gd on the microstructure and strength of Mg-4.5Zn alloy, Mater. Charact. 59 (2008) 1667-1674.
[51] H.W. Chen, C.L. Liu, Z.Q. Li, P. Li, A.P. Zhang, J.F. Nie, Effect of Ca addition on microstrcutres of aged Mg-15Gd-0.5Zr alloy, Mater. Charact. 159 (2019) 109838.
[52] J.F. Nie, K. Oh-Ishi, X. Gao, K. Hono, Solute segregation and precipitation in a creep-resistant Mg–Gd–Zn alloy, Acta Mater. 56 (20) (2008) 6061-6076.
[53] T. Bhattacharjee, C.L. Mendis, K. Oh-ishi, T. Ohkubo, K. Hono, The effect of Ag and Ca additions on the age hardening response of Mg-Zn alloys, Mater. Sci. Eng. A 575 (2013) 231-240.
[54] M.Z. Bian, T.T. Sasaki, T. Nakata, Y. Yoshida, N. Kawabe, S. Kamado, K. Hono, Bake-hardenable Mg-Al-Zn-Mn-Ca sheet alloy processed by twin-roll casting, Acta Mater. 158 (2018) 278-288.
[55] M. Nishijima, K. Hiraga, Structural changes of precipitates in an Mg-5at%Gd alloy studied by transmission electron microscopy, Mater. Trans. 48 (2007) 10-15.
[56] J.P. Hadorn, T.T. Sasaki, T. Nakata, T. Ohkubo, S. Kamado, K. Hono, Solute clustering and grain boundary segregation in extruded dilute Mg-Gd alloys, Scr. Mater. 93 (2014) 28-31.
[57] A.R. Natarajan, E.L.S. Solomon, B. Puchala, E.A. Marquis, A. Van der Ven, On the early stages of precipitation in dilute Mg-Nd alloys, Acta Mater. 108 (2015) 367-379.
[58] J.K. Zheng, R. Luo, X. Zeng, B. Chen, Nano-scale precipitation and phase growth in Mg-Gd binary alloy: An atomic-scale investigation using HAADF-STEM, Mater. Des. 137 (2018) 316-324.
[59] Y. Zhang, W. Rong, Y. Wu, L. Peng, J.F. Nie, N. Birbilis, A detailed HAADF-STEM study of precipitate evolution in Mg-Gd alloy, J. Alloys Compd. 777 (2019) 531-543.
[60] J.F. Nie, N.C. Wilson, Y.M. Zhu, Z. Xu, Solute clusters and GP zones in binary Mg–RE alloys, Acta Mater. 106 (2016) 260-271.
[61] J.C. Slater, Atomic radii in crystals, J. Chem. Phys. 10 (1964) 3199-3204.

[62] M.J. Starink, S.C. Wang, The thermodynamics of and strengthening due to co-clusters: General theory and application to the case of Al-Cu-Mg alloys, Acta. Meter. 57 (2009) 2376-2389.
[63] J.C. Fisher, On the strength of solid solution alloys, Acta Metall. 2 (1954) 9-10.
[64] P.A. Flinn, Solute hardening of close-packed solid solutions, Acta Metall. 6 (1958) 631-635.
[65] S. Abaspour, C.H. Cáceres, Thermodynamics-based selection and design of creep-resistant cast Mg alloys, Metall. Mater. Trans. A, 46 (12) (2015) 5972-5988.
[66] G. Thomas, The effect of short-range order on stacking fault energy and dislocation arrangements in f.c.c. solid solutions, Acta Metall. 11 (1963) 3169-1371.
[67] V. Gerold, H.P. Karnthaler, On the origin of planar slip in F.C.C. Alloys, Acta Metall. 37 (8) (1989) 2177-2183.
[68] A. Marucco, Atomic ordering and α′-Cr phase precipitation in long-term aged Ni3Cr and Ni2Cr alloys, J. Mater. Sci. 30 (16) (1995) 4188-4194.
[69] T. Neeraj, D.H. Hou, G.S. Daehn, M.J. Mills, Phenomenological and microstructural analysis of room temperature creep in titaium alloys, Acta Mater. 48 (2000) 1225-1238.
[70] T. Neeraj, M.J. Mills, Short-range order (SRO) and its effect on the primary creep behaviour of a Ti-6wt.%Al alloy, Mater. Sci. Eng. A 319 (2001) 415-419.
[71] P. Castany, F.Pettinari-Sturmel, J. Douin, A. Coujou, TEM quantitative characterization of short-range order and its effects on the deformation micromechanisms in a Ti-6Al-4V alloy, Mater. Sci. Eng. A 680 (2017) 85-91.
[72] M. Suzuki, T. Kimura, J. Koike, K. Maruyama, Strengthening effect of Zn in heat resistant Mg-Y-Zn solid solution alloys, Scr. Mater. 48 (2003) 997-1002.
[73] W. Blum, Creep of crystalline materials: experimental basis, mechanisms and models, Mater. Sci. Eng. A 319 (2001) 8-15.
[74] L. Hu, L. Zhan, R. Shen, Z. Liu, Z. Ma, J. Liu, Y. Yang, Effect of uniaxial creep ageing on the mechanical properties and micro precipitates of Al-Li-S4 alloy, Mater. Sci. Eng. A 688 (2017) 272-279.
[75] R. Li, J. Zhang, G. Fu, L. Zong, B. Guo, Y. Yu, Y, Su, Y. Hao, Different precipitation hardening behaviors of extruded Mg-6Gd-1Ca alloy during artifical aging and creep processes, Mater. Sci. Eng. A 715 (2018) 186-193.